光学学报

势能助力靶原子离化激发辐射近红外光谱

张颖[1,2]，徐忠峰[2]，王兴[2]，任洁茹[2]，张艳宁[1]，梅策香[1]，周贤明[1]，梁昌慧[1]，王伟[3]，张小安[1,3*]

[1]咸阳师范学院离子束与光物理实验室，陕西 咸阳 712000；
[2]西安交通大学物理学院，陕西 西安 710049；
[3]中国科学院近代物理研究所，甘肃 兰州 730000

摘要 用动能为 1360 keV 的 $^{129}Xe^{q+}$（$q=17,20,23,25,27$）高电荷态离子分别入射到金属 Al 和 Ti 固体靶表面，测量高电荷离子与表面相互作用过程中离子俘获表面电子完成中性化所形成的激发态 Xe 原子和低电离态 Xe 离子退激辐射的近红外光谱线（800～1700 nm），以及靶原子被离化激发、退激辐射的光谱线。实验结果表明：高电荷态离子入射金属表面的过程中，携带的势能在飞秒量级的时间内沉积到靶表面，使靶原子离化激发，较强的库仑势能可使靶原子形成高离化态和复杂的电子组态、退激辐射光谱线。随着入射离子的电荷态增加，测量谱线的强度增大，该变化趋势与入射离子的势能随电荷增加的变化趋势大体一致，说明经典过垒模型在近玻尔速度能区是成立的。

关键词 原子与分子物理学；高电荷态离子；经典过垒模型；禁戒跃迁；近红外光谱

中图分类号 O571.33　　**文献标志码** A　　　　　　　　　　**DOI：** 10.3788/AOS231910

1 引　言

高电荷重离子的势能是其电离能的总和（以 Xe^{q+} 为例，其势能 $U(q)=\sum_{i=1}^{q}I_i$，I_i 为 Xe 原子每电离一次的电离能）。具有一定动能的高电荷态离子入射到固体靶表面时发生弹性和非弹性散射，出现了许多新奇的现象，受到相关国际著名实验室的高度关注。1950 年代，美国 Bell 实验室的 Hagstrum[1] 首次提出单电荷态、重离子入射金属固体表面的 Auger 电子发射理论。随着研究的深入，该实验室的 White 和 Tolk[2] 于 1971 年首次给出此相互作用过程中被激发的靶原子光辐射退激的辐射函数。

随着科学技术的进步，可以实现高原子序数（Z）的多电子剥离，由于高电荷态离子可以产生很强的库仑场，例如 U^{91+} 的库仑场强度可达到 10^{16} V/cm，这是目前外场无法实现的[3-4]，因此高电荷态重离子与固体靶的作用成为研究热点之一。研究表明，高电荷态离子入射到固体靶表面的过程中，离化激发靶原子退激辐射从近红外到 X 射线的特征光谱线、发射电子、使靶表面发生库仑爆炸等[5]。由于高电荷态离子与固体靶的相互作用是复杂的多离子体系，目前没有较为完善的理论。1991 年，美国橡树岭国家实验的 Burgdörfer 等[6] 提出一种离子速度低于玻尔速度的经典过垒模型；2017 年，Wilhelm 等[7] 研究得到 Auger 中性化速率为 10^{11}～10^{12} s^{-1}，靶原子间的库仑退激速率（ICD）为 10^{15} s^{-1}，这对基于 Auger 中性化的经典过垒模型提出了挑战，因此高电荷态离子与表面相互作用的研究有待深入。此外，高电荷态离子辐射的特征光谱线是聚变等离子体研究中重要的光学诊断方法之一[8-9]。随着我国科学技术的发展，兰州重离子加速器国家实验室建成的电子回旋共振离子源[10]（ECRIS）和复旦大学建成的上海电子束离子阱[11]（EBIT）装置，可提供束流动能可调范围大、单离子势能（电荷态 q）可以有多种选择的离子束。选择近玻尔速度能区的高电荷态离子与靶相互作用，可以在研究离子与靶相互作用时的束缚态能量演化中，忽略相对论效应和高 Z 离子量子电动力学（QED）效应的影响。Al 和 Ti 及它们的合金是航空航天器件的常用材料，太空中的高能粒子（电子、光子和高电荷态离子）会对器件造成次级电子发射、表面原子激发和粒子数反转等伤害，对其作用过程的研究是当前的重要工作之一[12-13]，Al^{1+} 和 Ti^{1+} 以及类 Ti 离子退激辐射的近红外光谱成为目前高精度光钟研究领域的热点[14]，而且红外背景辐射是研究宇宙演化的重要手段[15]。

本文基于兰州重离子加速器国家实验室电子回旋共振（ECR）离子源，将 $^{129}Xe^{q+}$（$E_0=1360$ keV，

$17 \ll q \ll 27$)离子分别入射到 Al 和 Ti 靶表面,测量相互作用过程发射的 800~1700 nm 的光谱线,验证经典过垒模型的适用性。所报道的实验数据能为相关研究提供基础数据支撑。

2 实验装置与测量方法

图 1 为兰州重离子加速器国家实验室的测量平台示意图。气态 ^{129}Xe 原子在 ECR 腔体中与电子在馈入 18 GHz 的微波场中反复碰撞,逐步剥离后形成高电荷态 ^{129}Xe^{q+} 离子,在实验所需的电压下引出。根据荷质比,利用分析磁铁选出实验需要的炮弹离子,通过聚束器、四极透镜和光阑控制束斑小于 5 mm,同时利用法

拉第筒记录束流强度,束流进入具有磁屏蔽的金属超高真空(真空度维持在 10^{-8} Pa)靶室。样品 Al、Ti 的化学纯度为 99.99%,表面经过净化处理,靶面积为 15 mm×15 mm,厚度为 0.1 mm。红外光学窗口和单色仪入射狭缝与束流方向垂直,且与靶表面成 45°角。实验用美国 ARC(Action Reserch Corporation)公司生产的红外谱仪 SP-2357,光栅密度为 600 g/mm,闪耀波长为 1.6 μm,选用 InGaA-C 探测器,其有效范围为 800~1700 nm,积分时间为 3000 ms。为了提高信噪比和测量精度,使用锁相放大器(SR830)和斩波器(SR540),并在暗室条件下完成整个实验,保证光谱测量的本底最小。
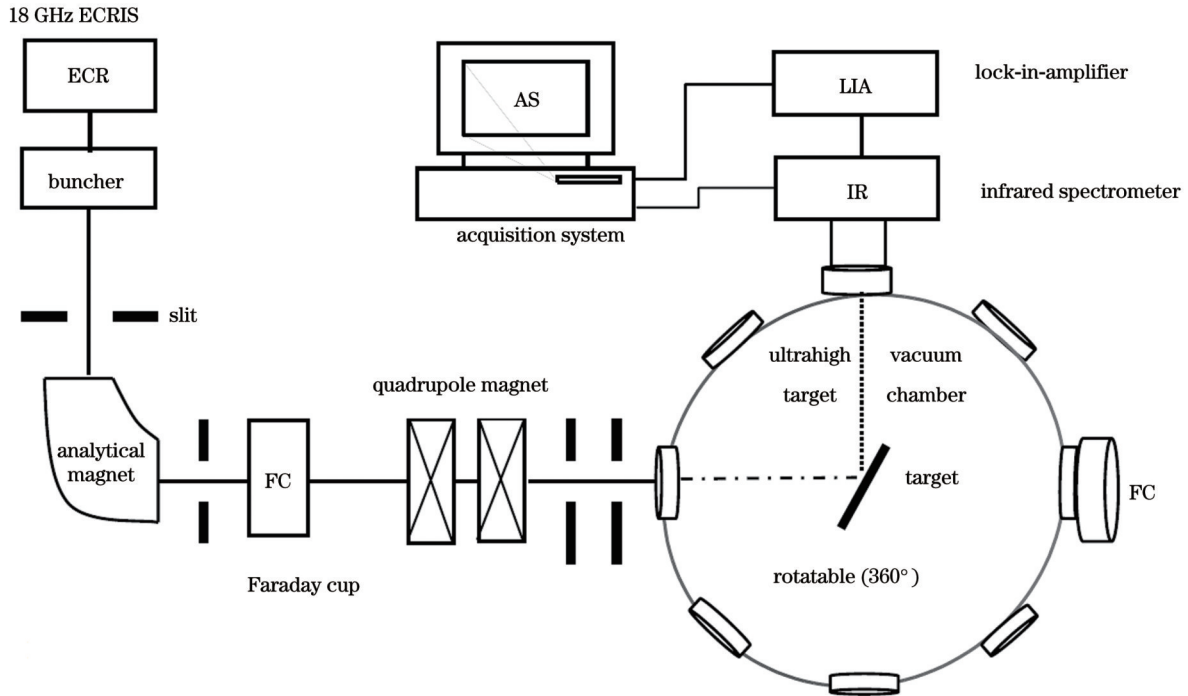

图 1 兰州重离子加速器国家实验室 ECR 离子源原子物理实验平台示意图

Fig. 1 Schematic for atomic physics platform on ECRIS in HIRFL

3 结果与讨论

3.1 动能一定、不同电荷态 ^{129}Xe^{q+} 离子束激发靶表面的近红外光谱线

选动能固定为 1360 keV,电荷态 $q+$ 分别为 17+、20+、23+、25+、27+ 的高电荷态离子分别入射 Al/Ti 靶表面,测量碰撞过程中发射的 800~1700 nm 近红外光谱线。图 2(a)、(b)所示分别为 ^{129}Xe^{17+} 和 ^{129}Xe^{27+} 离子入射 Al 靶的红外光谱线,图 3(a)、(b)所示分别为 ^{129}Xe^{17+} 和 ^{129}Xe^{27+} 离子入射 Ti 靶的红外光谱线。利用光谱图获取系统自带的程序扣除背景辐射,这可能会丢失一些有用的信息。谱线的归属依据是 NIST 数据库[16],图 2 和图 3 给出了相对较强的谱线。其中:Al I 1595.72 nm 是上能级 45194.681 cm^{-1}(电子组态为 3s^{2}6f,态项为 y ^{2}F°,总角动量子数为 5/2)到下能级

38929.413 cm^{-1}(电子组态 3s^{2}nd,态项为 y ^{2}D,总角动量子数为 3/2)的跃迁,跃迁速率为 $1.12×10^5$ s^{-1};Al XII(类 He-Al 离子,Al^{11+})1525.03 nm 是上能级 15836017 cm^{-1}(电子组态为 1s4d,态项为 ^{3}D,总角动量子数为 2)到下能级 15829460 cm^{-1}(电子组态为 1s4p,态项为 ^{3}P°,总角动量子数为 2)的跃迁,跃迁速率为 $1.74×10^5$ s^{-1};Al XI 1251.08 nm 是上能级 2734110 cm^{-1}(电子组态为 1s^{2}4d,态项为 ^{2}D,总角动量子数为 3/2)到下能级 2726120 cm^{-1}(电子组态为 1s^{2}4p,态项为 ^{2}P°,总角动量子数为 1/2);Al XII(类 He-Al 离子)842.42 nm 是上能级 15828659 cm^{-1}(电子组态为 1s4p,态项为 ^{3}P°,总角动量子数为 0)到下能级 15816791 cm^{-1}(电子组态为 1s4s,态项为 ^{3}S,总角动量子数为 1)的跃迁,其速率为 $4.17×10^6$ s^{-1};Al XI(类 Li-Al 离子,Al^{10+})1251.08 nm 是上能级 2734110 cm^{-1}(电子组态为

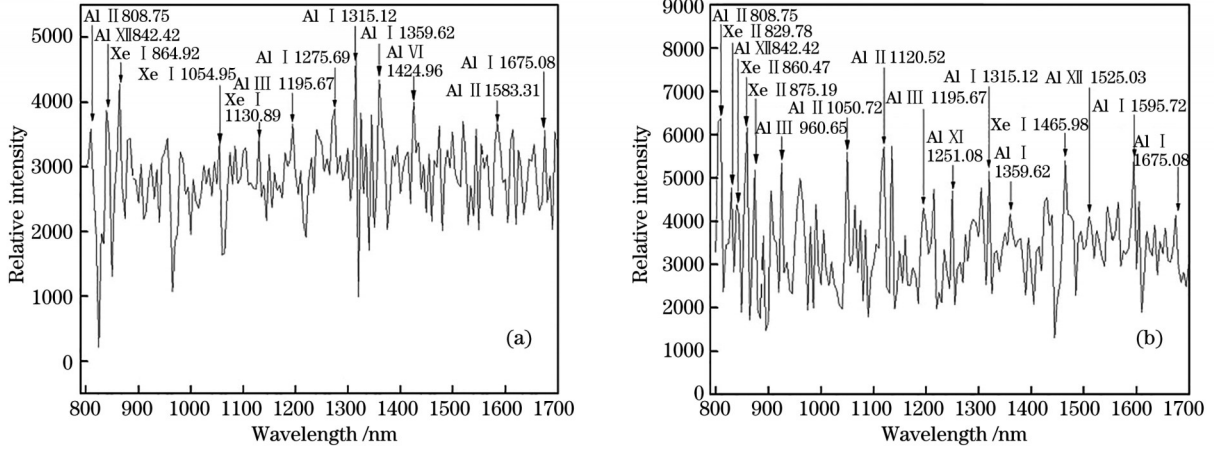图 2 动能一定（1360 keV）的 ^{129}Xe^{q+} 离子入射到 Al 靶表面时激发的近红外光谱。(a) ^{129}Xe^{17+}；(b) ^{129}Xe^{27+}

Fig. 2 Measured near-infrared spectra induced by ^{129}Xe^{q+} ions with 1360 keV kinetic energy impacting on Al surface. (a) ^{129}Xe^{17+}; (b) ^{129}Xe^{27+}
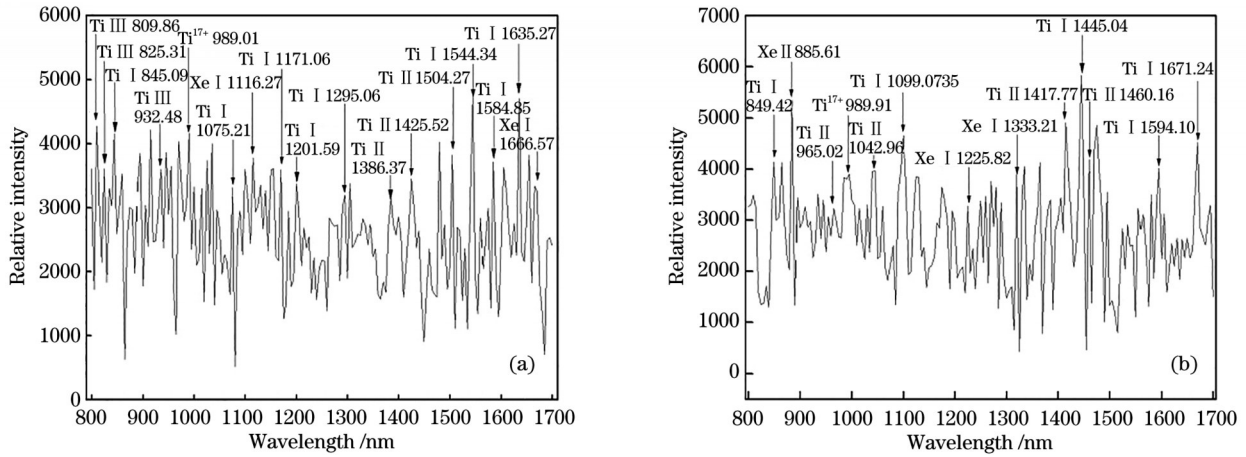
图 3 动能一定（1360 keV）的 ^{129}Xe^{q+} 离子入射到 Ti 靶表面时激发的近红外光谱。(a) ^{129}Xe^{17+}；(b) ^{129}Xe^{27+}

Fig. 3 Measured near-infrared spectra induced by ^{129}Xe^{q+} ions with 1360 keV kinetic energy impacting on Ti surface. (a) ^{129}Xe^{17+}; (b) ^{129}Xe^{27+}

1s^{2}4d，态项为 ^{2}D，总角动量子数为 3/2）到下能级 2726120 cm^{-1}（电子组态为 1s^{2}4p，态项为 ^{2}P°，总角动量子数为 1/2）的跃迁，跃迁速率为 1.23×10^6 s^{-1}。Ti XVIII（Ti^{17+}）989.01 nm 是上能级 1088900 cm^{-1}（电子组态为 2p^3，态项为 ^{2}D，总角动量子数为 3/2）到下能级 1078800 cm^{-1}（电子组态为 2p^3，态项为 ^{2}D°，总角动量子数为 5/2）的跃迁，属于磁偶极跃迁。相对强度较大的 Ti II 的谱线较多，如 Ti II 1520.52 nm 是上能级 71461.79 cm^{-1}[电子组态为 3d^2(^{3}F)5p，态项为 ^{4}G°，总角

动量子数为 5/2]到下能级 64886.67 cm^{-1}[电子组态为 3d^2(^{3}F)4d，态项为 e ^{4}G，总角动量子数为 5/2]的跃迁。

本实验测量到的高电荷态离子 ^{129}Xe^{q+} 在相互作用过程中俘获靶电子中性化处于激发态的 Xe I 和 Xe II 退激辐射的特征谱线较多，它们都属于电偶极跃迁辐射，如 Xe I 864.92 nm 和 Xe I 1465.92 nm 是同一上能级 88744.559 cm^{-1} 分别向下能级 77185.041 cm^{-1} 和 81925.514 cm^{-1} 跃迁时发射的谱线，详细的跃迁见表 1。

表 1 ^{129}Xe^{q+} 分别入射 Al、Ti 靶时激发的光谱数据

Table 1 Measured spectrum data induced by ^{129}Xe^{q+} ions on Al and Ti surface

Ion	Observed wavelength /nm	Reference wavelength[16] /nm	Upper level			Lower level			Transition type
			Configuration	Term	J	Configuration	Term	J	
Al II	808.75±0.03	808.69	3s9f	^{1}F°	3	3s5d	^{1}D	2	E$_1$
Al XII	842.42±0.01	842.40	1s4p	^{3}P°	0	1s4s	^{3}S	1	E$_1$
Al III	960.65±0.02	960.61	2p^{6}5d	^{2}D	5/2	2p^{6}5p	^{2}P°	3/2	E$_1$

续表

Ion	Observed wavelength /nm	Reference wavelength[16] /nm	Upper level			Lower level			Transition type
			Configuration	Term	J	Configuration	Term	J	
Al II	1050.72±0.01	1050.68	3s9s	^{3}S	1	3s6p	^{3}P°	0	E$_1$
Al II	1120.52±0.04	1120.44	3s7d	^{3}D	2	3s5f	^{3}F°	3	E$_1$
Al III	1195.67±0.02	1195.60	2p^{6}8d	^{2}D	3/2	2p^{6}7p	^{2}P°	1/2	E$_1$
Al XI	1251.08±0.02	1251.00	1s^{2}4d	^{2}D	3/2	1s^{2}4p	^{2}P°	1/2	E$_1$
Al I	1275.69±0.01	1275.73	3s^{2}5p	^{2}P°	1/2	3s^{2}3d	^{2}D	3/2	E$_1$
Al I	1315.12±0.01	1315.08	3s^{2}4p	^{2}P°	1/2	3s^{2}4s	^{2}S	1/2	E$_1$
Al I	1359.62±0.03	1359.57	3s7d	^{3}D	1	3s6p	^{3}P°	0	E$_1$
Al I	1424.96±0.02	1424.90	2s^{2}2p^3(^{2}P°)3s	^{3}P°	1	2s^{2}2p^3(^{4}S°)3p	^{3}P	1	E$_1$
Al II	1583.31±0.04	1583.25	3s8f	^{3}F°	2	3s6d	^{3}D	3	E$_1$
AlXII	1525.03±0.01	1525.00	1s4d	^{3}D	2	1s4p	^{3}P°	2	E$_1$
Al I	1595.72±0.02	1595.66	3s^{2}6f	^{2}F°	5/2	3s^{2}nd	y ^{2}D	3/2	E$_1$
Al I	1675.08±0.02	1675.05	3s^{2}nd	y ^{2}D	5/2	3s^{2}4p	^{2}P°	3/2	E$_1$
Ti III	809.86±0.04	809.85	3p^{6}3d5p	^{3}D°	2	3p^{6}3d4d	^{1}D	2	E$_1$
Ti III	825.31±0.04	825.29	3p^{6}3d5f	^{3}D°	3	3p^{6}3d5d	^{3}F	4	E$_1$
Ti I	845.09±0.04	845.08	3d^2(^{1}G)4s4p(^{3}P°)	x ^{3}G°	4	3d^3(^{2}H)4s	a ^{3}H	5	E$_1$
Ti III	932.49±0.01	932.48	3p^{6}3d^2	^{3}P	2	3p^{6}3d^2	^{3}F	2	E$_2$ M$_2$
Ti II	965.02±0.01	965.00	3d^2(^{1}G)4s	b ^{2}G	9/2	3d^2(^{3}F)4s	a ^{2}F	7/2	E$_2$ M$_2$
Ti XVIII	989.01±0.01	989.00	2p^3	^{2}D°	3/2	2p^3	^{2}D°	5/2	M$_1$
Ti I	1075.21±0.03	1075.18	3d^4	^{3}P$_2$	0	3d^2(^{3}P)4s4p(^{3}P°)	z ^{3}S°	1	E$_1$
Ti I	1171.04±0.04	1171.06	3d^2(^{1}D)4s4p(^{3}P°)	x ^{3}D°	1	3d^3(^{4}P)4s	c ^{3}P	0	E$_1$
Ti I	1201.08±0.03	1201.06	3d^4	^{3}F$_2$	2	3d^2(^{1}D)4s4p(^{3}P°)	x ^{3}F°	2	E$_1$
Ti I	1295.06±0.04	1295.09	3d^4	^{3}H	6	3d^2(^{3}F)4s4p(^{1}P°)	y ^{3}G°	5	E$_1$
Ti II	1386.37±0.02	1386.35	3d^2(^{3}F)5p	^{4}D°	7/2	3d^2(^{3}F)5p	^{4}D	5/2	E$_1$
Ti II	1425.52±0.02	1425.49	3d^2(^{3}F)4f	^{2}H°	9/2	3d^2(^{1}D)4d	^{2}G	7/2	E$_1$
Ti X	1445.82±0.01	1445.90	3s3p^2	^{4}P	5/2	3s3p^2	^{4}P	1/2	E$_2$
Ti II	1504.27±0.02	1504.26	3d^2(^{3}F)5p	^{4}F°	7/2	3d^2(^{3}F)4d	f ^{2}F	5/2	E$_1$
Ti II	1520.52±0.02	1520.47	3d^2(^{3}F)5p	^{4}G°	5/2	3d^2(^{3}F)4d	e ^{4}G	5/2	E$_1$
Ti I	1544.34±0.02	1544.28	3d^{2}4s(^{4}F$_{7/2}$)4f	^{2}[7/2]°	4	3d^{2}4s(^{4}F)4d	e ^{5}G	3	E$_1$
Ti II	1425.52±0.02	1425.49	3d^2(^{3}F)4f	^{2}H°	9/2	3d^2(^{1}D)4d	^{2}G	7/2	E$_1$
Ti I	1584.85±0.05	1584.83	3d^{2}4s(^{4}F$_{7/2}$)4f	^{2}[9/2]°	5	3d^{2}4s(^{4}F)4d	e ^{5}H	4	E$_1$
Ti I	1635.27±0.03	1635.21	3d^{2}4s(^{4}F$_{7/2}$)4f	^{2}[3/2]°	2	3d^{2}4s(^{4}F)4d	e ^{5}D	1	E$_1$
Xe II	829.78±0.02	829.76	5s^{2}5p^4(^{3}P$_0$)5g	^{2}[4]	9/2	5s^{2}5p^4(^{3}P$_0$)4f	^{2}[3]°	7/2	E$_1$
Xe I	855.97±0.03	855.94	5p^5(^{2}P°$_{3/2}$)9p	^{2}[5/2]	2	5p^5(^{2}P°$_{3/2}$)5d	^{2}[5/2]°	3	E$_1$
Xe II	860.47±0.04	860.42	5s^{2}5p^4(^{3}P$_2$)5g	^{2}[6]	11/2	5s^{2}5p^4(^{3}P$_2$)4f	^{2}[5]°	9/2	E$_1$
Xe I	864.92±0.04	864.85	5p^5(^{2}P°$_{3/2}$)7p	^{2}[3/2]	1	5p^5(^{2}P°$_{1/2}$)6s	^{2}[1/2]°	1	E$_1$
Xe II	875.19±0.02	875.21	5s^{2}5p^4(^{3}P$_2$)5g	^{2}[4]	9/2	5s^{2}5p^4(^{3}P$_2$)4f	^{2}[4]°	7/2	E$_1$
Xe I	979.95±0.06	979.97	5p^5(^{2}P°$_{3/2}$)6p	^{2}[1/2]	1	5p^5(^{2}P°$_{3/2}$)6s	^{2}[3/2]°	2	E$_1$
Xe I	1054.95±0.03	1054.97	5p^5(^{2}P°$_{3/2}$)5f	^{2}[3/2]	2	5p^5(^{2}P°$_{3/2}$)5d	^{2}[3/2]°	1	E$_1$
Xe I	1130.89±0.03	1130.96	5p^5(^{2}P°$_{1/2}$)6p	^{2}[3/2]	2	5p^5(^{2}P°$_{3/2}$)5d	^{2}[3/2]°	2	E$_1$
Xe I	1465.92±0.05	1465.98	5p^5(^{2}P°$_{3/2}$)7p	^{2}[3/2]	1	5p^5(^{2}P°$_{3/2}$)5d	^{2}[5/2]°	2	E$_1$
Xe I	1666.57±0.05	1666.51	5p^5(^{2}P°$_{3/2}$)8d	^{2}[3/2]°	1	5p^5(^{2}P°$_{3/2}$)7p	^{2}[3/2]	2	E$_1$

3.2 讨 论

动能为 1360 keV 的 $^{129}\text{Xe}^{q+}$ 炮弹离子分别入射到 Al 和 Ti 金属固体靶表面，其速度约为 1.42×10^{6} m/s（小于玻尔速度 $V_{\text{Bohr}}=2.19\times10^{6}$ m/s，Al 靶的脱出功为 $\varphi_{\text{Al}}=4.28$ eV，Ti 靶的脱出功为 $\varphi_{\text{Ti}}=4.33$ eV），当到达靶的表面上方、垂直于靶表面的临界距离为 R_{C} 时，开始共振俘获靶表面的中性化电子[5]。

$$R_{\text{C}}=\frac{\sqrt{8q}}{2\varphi}。\tag{1}$$

俘获电子进入炮弹离子轨道的主量子为

$$n_{\text{C}}=\frac{q}{\sqrt{2\varphi}}\times\frac{1}{\sqrt{1+\dfrac{q-0.5}{\sqrt{8q}}}}。\tag{2}$$

式（1）和（2）均采用原子单位（a.u.）。例如：对于铝靶，入射离子的电荷态 $q=17$ 时，$R_{\text{C}}\approx37$ a.u，$n_{\text{C}}\approx21$，而 $q=27$ 时，$R_{\text{C}}\approx47$ a.u，$n_{\text{C}}\approx29$；对于钛靶，入射离子的电荷态 $q=17$ 时，$R_{\text{C}}\approx36$ a.u，$n_{\text{C}}\approx19$，而 $q=27$ 时，$R_{\text{C}}\approx46$ a.u，$n_{\text{C}}\approx28$。入射离子从临界表面到撞击表面靶原子的时间为

$$t=\frac{R_{\text{C}}}{v}=\frac{37\times0.53\times10^{-10}\ \text{m}}{1.42\times10^{6}\ \text{m/s}}=1.38\times10^{-15}\ \text{s}。\tag{3}$$

对于 Al 和 Ti 靶，由式（3）可知，从 $q=17$ 到 $q=27$，入射离子在靶表面经历的时间都为 10^{-15} s 量级，从共振俘获靶导带电子开始中性化，释放势能使靶原子离化激发，靶原子处于较强的库仑场中，较高能级的简并将会解除或部分解除，同时炮弹离子一般也处于激发态。此外，由于高电荷态离子 $^{129}\text{Xe}^{q+}$ 在入射到金属靶表面时，会引起靶表面导带电子集体响应，形成高电荷态离子的像电荷，产生的能量增益[17]为

$$\Delta E=\frac{\varphi q^{3/2}}{4\sqrt{2}}。\tag{4}$$

炮弹离子将携带的能量［动能 1360 keV、势能 $U(q)$ 和增益的能量］瞬间释放［按照式（3）的计算，入射离子与靶相互作用的时间为飞秒量级］于靶表面，使 Al 靶（或 Ti 靶）的原子离化激发，退激辐射出复杂光谱线。炮弹离子俘获的电子先进入主量子数为 n_{C} 的壳层，按照级联方式退激辐射出红外光谱线、可见光谱线、紫外光谱线和 X 射线[18]。

Xe^{1+} 离子和 Xe 原子的谱线来自入射的高电荷态 $^{129}\text{Xe}^{q+}$ 离子按照以上共振俘获靶电子中性化过程中退激辐射的光谱线。Al 和 Ti 靶是相对较好的导体，在入射离子库仑场中可被靶表面电子瞬时中性化，因此没测到更高电荷态 Xe 离子退激辐射的光谱线，但测量得到此库仑场作用下靶原子离化激发时退激辐射的光谱线，如类氢（Al XII）Al 离子（即 Al^{11+}）辐射的 842.42 nm 和 1525.03 nm 谱线以及类锂（Al XI）Al（Al^{10+}）离子的 1251.08 nm 谱线都来自电偶极跃迁辐射，是 Fernley

等[19]于 1987 年采用量子密耦方法计算得到的，Ti XVIII（即 Ti^{17+}）退激辐射的 989.01 nm 光谱线来自磁偶极跃迁辐射，由 Jönsson 等[20]于 2013 年用相对论组态相互作用方法计算得到，但是这些高离化态靶离子的谱线至今没有实验数据报道。同时，本实验测量到 Ti^{2+} 退激辐射的 932.49 nm 光谱线和 Ti^{1+} 965.02 nm 光谱线来自偶极禁戒跃迁，该跃迁属于电四极辐射和磁偶极跃迁辐射，在近红外光波段存在电四极辐射和磁偶极跃迁辐射的竞争[21]。从表 1 的实验结果看，入射离子俘获表面电子形成的 Xe 原子或 Xe 离子的激发态、靶原子 Al 和 Ti 或离子的激发态大多是在非弹性散射过程中，强库仑场引起原子或离子能态的多重简并被解除，发生精细结构分裂，其间的跃迁辐射产生近红外光谱线。总之，传统的光激发、放电法或电子碰撞方法等难以实现能离化并激发原子或离子复杂组态之间的光谱线[22]。

在测量的谱线中，相对较强的谱线为靶原子被离化和激发、其离化态较低（Al^{3+}、Al^{2+}、Ti^{3+}、Ti^{2+}）的离子退激辐射的近红外光谱线和激发的靶原子退激辐射的光谱线。为了进一步分析谱线的相对强度与入射离子电荷态 q 之间的关系，消除入射离子束流强度波动的影响，引入单离子荧光产额[23]：

$$Y_{\text{IF}}\approx\frac{R}{N},\ N=\frac{I}{q\cdot e}\cdot\Delta t，\tag{5}$$

式中：R 表示谱线的相对强度；N 为入射离子总数；I 为束流强度；Δt 为积分时间。

图 4 所示为根据式（5）计算的单离子荧光产额和入射离子所携的势能随入射离子电荷态的变化关系。可以看到，Al XII 842.42 nm 的单离子荧光产额相对较大，Ti III 932.49 nm 的最小，这是因为类氢（Al XII）Al 离子的两个电子之间以及两个电子与原子核之间的库仑作用［吸引能 $-Z^2e^2/a_0=-4.598$ keV，
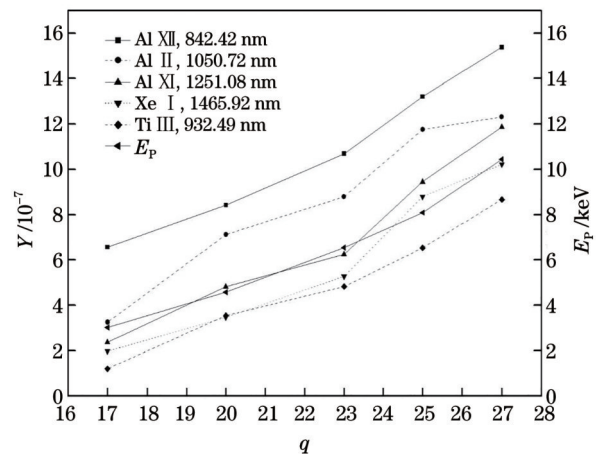

图 4 近红外光谱线的单离子产额和 $^{129}\text{Xe}^{q+}$（$q=17\sim27$）离子携带势能随电荷态增加的趋势

Fig. 4 Single ion fluorescence yield of near-infrared spectra and potential energy of $^{129}\text{Xe}^{q+}$ ion as functions of charge q

排斥能 $(5/8)(Ze^2/a_0) = 221.09\ \text{eV}$] 起主要作用，自旋和轨道耦合使三重态简并解除，能级分裂，简言之，上能级 1s4p 向下能级 1s4s 退激辐射产生 842.42 nm 光谱线，上能级 1s4d 向下能级 1s4p 退激辐射产生 1525.03 nm 谱线，离化激发的类锂（Al XI）（Al^{10+}）Al 离子上能级 $1s^24d$ 向下能级 $1s^24p$ 退激辐射产生 1251.08 nm 谱线，这些能级分裂较小，电偶极跃迁辐射概率很大，所发射的谱线较强。Ti III 的谱线来自电四极辐射，谱线强度相对较小[24-25]。所有谱线的单粒子荧光产额随入射离子电荷增加的趋势与入射离子的势能 E_P（即总的离化能）随电荷态增加的趋势基本一致，说明在近玻尔速度的高电荷态离子入射金属靶表面的过程中，所携带的库仑势能沉积在靶表面，使靶原子激发离化，从而出现复杂组态间的跃迁。此外，当入射离子流强度一定时，$^{129}Xe^{q+}$ 离子的电荷态 q 越大，瞬时俘获靶电子的概率越大，中性化后形成激发态的 Xe I 原子和 Xe II 离子数量越多，辐射谱线越强，同时离化激发靶原子的数量也越多。对于 Ti 靶，其导带电子的脱出功 $\varphi_{Ti} = 4.33\ \text{eV}$ 大于 Al 靶的 $\varphi_{Al} = 4.28\ \text{eV}$，在外场作用下其电子移出表面的电流密度由 Richardson-Dushmon 公式[26-27]确定：

$$j = 4\pi e \frac{m(k_B)^2}{h^3} T^2 \exp\left(-\frac{\varphi}{k_B T}\right), \tag{6}$$

式中：k_B 为玻尔兹曼常数；h 为普朗克常数；e 为电子电量；m 为电子质量；T 为金属的温度。从式（6）可以看到，在相同的温度下，移出电子数取决于金属的脱出功，脱出功越大，移出电子数越少。因此，本实验在 Ti 表面测到的 Xe 原子或 Xe 离子的谱线以及 Ti 原子或 Ti 离子谱线中，大部分谱线的单离子荧光产额小于 Al 靶表面。

光谱测量容易受到环境以及发光体自身状态的影响，精确测量光谱是相关研究者一直探索的科学目标[28-31]。本实验尽管在暗室环境下进行，实验数据处理时用获取系统扣除本底，谱线的误差在 0.01～0.06 nm，主要来源于入射离子束流强度的波动，高电荷态离子与靶原子作用过程中的多重离化效应[32]。

4 结 论

高电荷态离子入射到金属固体靶面，在飞秒时间尺度内将携带的能量沉积到靶表面纳米空间，使靶原子离化激发，退激辐射光谱线，其中一些谱线是复杂电子组态间的跃迁，发生较强的电偶极禁戒跃迁。测量的谱线相对强度（单离子荧光产生额）随入射离子电荷态的增加而增大，增大的趋势与入射离子的势能随电荷增大的趋势大体一致，说明经典过垒模型在入射离子的动能在近玻尔速度能区是成立的。与气体靶原子的碰撞发生弹性和非弹性散射的研究方法不同，由于高电荷态离子入射固体表面产生了许多新奇的现象，如 Auger 过程和 ICD 过程的争议、靶原子的多重离

化引起的能移、入射离子具有总能量和增益能量的耗散通道等问题的研究还有待深入，谨祈望本工作能为相关研究提供基础数据支撑，为光谱测量提供新的方法参考。

参 考 文 献

[1] Hagstrum H D. Theory of auger ejection of electrons from metals by ions[J]. Physical Review, 1954, 96(2): 336-365.

[2] White C W, Tolk N H. Optical radiation from low-energy ion-surface collisions[J]. Physical Review Letters, 1971, 26(9): 486-489.

[3] Gillaspy J D. Highly charged ions[J]. Journal of Physics B, 2001, 34(19): R93-R130.

[4] 曾丽珊, 余谢秋, 田野. 从太赫兹波到光波驱动的集成电子加速器研究进展[J]. 中国激光, 2023, 50(17): 1714008.
Zeng Y S, Yu X Q, Tian Y. Research advances in integrated electron accelerators driven by spectrum band from terahertz to optical waves[J]. Chinese Journal of Lasers, 2023, 50(17): 1714008.

[5] Schenkel T, Hamza A V, Barnes A V, et al. Interaction of slow, very highly charged ions with surfaces[J]. Progress in Surface Science, 1999, 61(2/3/4): 23-84.

[6] Burgdörfer J, Lerner P, Meyer F W. Above-surface neutralization of highly charged ions: the classical over-the-barrier model[J]. Physical Review A, 1991, 44(9): 5674-5685.

[7] Wilhelm R A, Gruber E, Schwestka J, et al. Interatomic coulombic decay: the mechanism for rapid deexcitation of hollow atoms[J]. Physical Review Letters, 2017, 119(10): 103401.

[8] Atzeni S, Meyer-ter-Vehn J. 惯性聚变物理[M]. 沈百飞, 译. 北京: 科学出版社, 2008: 297-305.
Atzeni S, Meyer-ter-Vehn J. Physics of inertial fusion[M]. Shen B F, Transl. Beijing: Science Press, 2008: 297-305.

[9] 段斌, 吴泽清, 王建国. 惯性约束聚变等离子体的光谱诊断（I）[J]. 中国科学 G 辑, 2009, 39(1): 43-51.
Duan B, Wu Z Q, Wang J G. Spectral diagnosis of inertial confinement fusion plasma[J]. Science in China Series G, 2009, 39(1): 43-51.

[10] Zhao H W, Sun L T, Guo J W, et al. Intense highly charged ion beam production and operation with a superconducting electron cyclotron resonance ion source[J]. Physical Review Accelerators and Beams, 2017, 20(9): 094801.

[11] Ren B H, Xia Z H, Zhang Y, et al. Three-body fragmentation mechanism of $C_2H_4^{3+}$ produced by 18-keV/u Ne^{8+} impact[J]. Physical Review A, 2021, 104(2): 022811.

[12] Durante M, Cucinotta F A. Physical basis of radiation protection in space travel[J]. Reviews of Modern Physics, 2011, 83(4): 1245-1281.

[13] Peng X, Chen M S, Liu H. Optical emission spectrometric diagnosis of laser-induced plasma and shock front produced at moderate pressure[J]. Chinese Optics Letters, 2023, 21(2): 023001.

[14] Safronova M S, Budker D, DeMille D, et al. Search for new physics with atoms and molecules[J]. Reviews of Modern Physics, 2018, 90(2): 025008.

[15] Kashlinsky A, Arendt R G, Atrio-Barandela F, et al. Looking at cosmic near-infrared background radiation anisotropies[J]. Reviews of Modern Physics, 2018, 90(2): 025006.

[16] NIST. Atomic Spectra Database: NIST Standard Reference Database 78[EB/OL]. [2023-11-09]. https://www.nist.gov/pml/atomic-spectra-database.

[17] Burgdörfer J, Meyer F. Image acceleration of multiply charged ions by metallic surfaces[J]. Physical Review A, 1993, 47(1): R20-R22.

[18] Winter H, Aumayr F. Hollow atoms[J]. Journal of Physics B,

1999，32(1):R39-R65.

[19] Fernley J A, Taylor K T, Seaton M J. Atomic data for opacity calculations. VII. Energy levels, f values and photoionisation cross sections for He-like ions[J]. Journal of Physics B, 1987, 20 (23): 6457-6476.

[20] Jönsson P, Ekman J, Gustafsson S, et al. Energy levels and transition rates for the boron isoelectronic sequence: Si X, Ti XVIII-Cu XXV[J]. Astronomy & Astrophysics, 2013, 559: A100.

[21] 曾谨言. 量子力学-卷Ⅱ[M]. 3 版. 北京：科学出版社，2000: 655-660.
Zeng J Y. Quantum mechanics: Volume Ⅱ[M]. 3rd ed. Beijing: Science Press, 2000: 655-660.

[22] Vinko S M, Ciricosta O, Preston T R, et al. Investigation of femtosecond collisional ionization rates in a solid-density aluminium plasma[J]. Nature Communications, 2015, 6: 6397.

[23] Leung S Y, Tolk N H, Heiland W, et al. Optical radiation from low-energy hydrogen atomic and molecular ion-surface collisions [J]. Physical Review A, 1978, 18(2): 447-451.

[24] 杨福家. 原子物理学[M]. 4 版. 北京：高等教育出版社，2008: 235-239.
Yang F J. Atomic physics[M]. 4th ed. Beijing: Higher Education Press, 2008: 235-239.

[25] 徐克尊. 高等原子分子物理学[M]. 北京：科学出版社，2002: 120-125.
Xu K Z. Advanced atomic and molecular physics[M]. Beijing: Science Press, 2002: 120-125.

[26] 方俊鑫，陆栋. 固体物理学[M]. 上海：上海科学技术出版社，1980: 193-199.

Fang J X, Lu D. Solid state physics[M]. Shanghai: Shanghai Scientific & Technical Publishers, 1980: 193-199.

[27] Zeng L X, Zhou X M, Cheng R, et al. Temperature and energy effects on secondary electron emission from SiC ceramics induced by Xe^{17+} ions[J]. Scientific Reports, 2017, 7(1): 6482.

[28] 蔡亚超，步扬，王远航，等. 空间约束对激光诱导等离子体演化和光谱的影响[J]. 光学学报，2023，43(7): 0730001.
Cai Y C, Bu Y, Wang Y H, et al. Effect of spatial confinement on plasma evolution and spectrum in laser-induced breakdown spectroscopy[J]. Acta Optica Sinica, 2023, 43(7): 0730001.

[29] 黄文文，彭小红，李丽圆，等. 相机标定方法及进展研究综述[J]. 激光与光电子学进展，2023，60(16): 1600001.
Huang W W, Peng X H, Li L Y, et al. Review of camera calibration methods and their progress[J]. Laser & Optoelectronics Progress, 2023, 60(16): 1600001.

[30] Wang Q Q, Tan J Q, Jie Q, et al. Perturbation-driven echo-like superfluorescence in perovskite superlattices[J]. Advanced Photonics, 2023, 5(5): 055001.

[31] 杨翙勃，钱静，于潇涵，等. 超快激光微加工表面瞬态温度的黑体辐射法测量[J]. 中国激光，2023，50(24): 2402204.
Yang H B, Qian J, Yu X H, et al. Transient temperature measurement of ultrafast laser surface micro-processing via blackbody radiation method[J]. Chinese Journal of Lasers, 2023, 50(24): 2402204.

[32] 王兴，赵永涛，程锐，等. 重离子轰击 Ta 靶引起的多电离效应[J]. 物理学报，2012，61(19): 193201.
Wang X, Zhao Y T, Cheng R, et al. Multiple ionization effect of Ta induced by heavy ions[J]. Acta Physica Sinica, 2012, 61 (19): 193201.

Potential-Assisted Target Atomic Ionization Excitation Radiation Near-Infrared Spectra

Zhang Ying[1,2], Xu Zhongfeng[2], Wang Xing[2], Ren Jieru[2], Zhang Yanning[1], Mei Cexiang[1], Zhou Xianming[1], Liang Changhui[1], Wang Wei[3], Zhang Xiaoan[1,3*]

[1]*Ion Beam and Optical Physical Laboratory, Xianyang Normal University, Xianyang 712000, Shaanxi, China;*
[2]*School of Physics, Xi'an Jiaotong University, Xi'an 710049, Shaanxi, China;*
[3]*Institute of Modern Physics, Chinese Academy of Sciences, Lanzhou 730000, Gansu, China*

Abstract

Objective $^{129}Xe^{q+}$ ($q=17$, 20, 23, 25, 27) highly charged ions with a kinetic energy of 1360 keV are incident on the surface of metal Al and Ti solid targets respectively. The near-infrared spectral lines (800–1700 nm) of excited Xe atoms and low ionized Xe ions, and the spectral lines of excited target atoms and excited by ionization are measured during the interaction between the highly charged ions and the surface to achieve surface electron neutralization. The experimental results show that during the process of high charged ion incident on the metal surface, the potential energy carried by the ion instantly (in the femtosecond range) deposits on the target surface, ionizing and exciting the target atoms. Due to the strong Coulomb potential energy, the target atoms can form a highly ionized state and complex electronic configuration to de-excite the emission spectrum. As the charge state of the incident ion increases, the measured spectral line intensity rises, and the increasing trend is generally consistent with the growing trend of the potential energy of the incident ion, which indicates that the classical over-the-barrier model is valid in the near Bohr velocity energy region. We also hope that our experimental data can provide basic support for related research and provide new methods for spectral measurement.

Methods The experiment is performed at the Heavy Ion Research Facility in Lanzhou (HIRFL) and the experimental platform is shown in Fig. 1. Gaseous ^{129}Xe atoms repeatedly collide with electrons in an 18 GHz microwave field in the

ECR, gradually peeling off to form highly charged $^{129}Xe^{q+}$ ions. They are introduced at the required voltage for the experiment, and the required projectile ions are selected by analytical magnets based on the charge-to-mass ratio. The beam spot is controlled to be less than 5 mm using a beam splitter, quadrupole lens, and aperture, and the beam intensity is recorded via a Faraday tube. The beam enters a metal ultra-high vacuum chamber with magnetic shielding (vacuum degree maintained at 10^{-8} Pa). The chemical purity of sample Al or Ti is 99.99%, and the surface has been purified with a target area of 15 mm×15 mm and thickness of 0.1 mm. The infrared optical window and monochromator incident slit are perpendicular to the beam direction and form a 45° angle with the target surface. The experiment employs an infrared spectrometer SP-2357 produced by ARC (Action Reserve Corporation) in the United States, with a grating density of 600 g/mm and a flashing wavelength of 1.6 μm. The InGaA-C detector is selected with an effective range of 800−1700 nm and an integration time of 3000 ms. To improve the signal-to-noise ratio and measurement accuracy, we adopt a phase-locked amplifier (SR830) and a chopper (SR540). Additionally, we have to operate in the darkroom or the dark cover screening to eliminate or reduce the background of spectral measurement.

Results and Discussions   The near-infrared spectral lines (800−1700 nm) emitted from the interaction between high charge state $^{129}Xe^{q+}$ ($q=17-27$) and metal solid targets are measured (Table 1). These spectral lines can be adopted in the research on the damage of space-charged particles to aerospace devices, high-precision optical clocks, and in the infrared background radiation of the universe in laboratory astrophysics. Xe ion emission near-infrared is an important basis for manipulating Hall thrusters, with space stations performing attitude calibration and other actions in space.

Under the action of highly charged ions, it is possible to ionize and excite transitions between complex configurations of target atoms, and electric dipole forbidden transitions (magnetic dipole and electric quadrupole transitions). Additionally, we measure spectral lines of 842.42 nm and 1525.03 nm for helium like (Al XII) Al ions (*i.e.* Al^{11+}) radiation, and 1251.08 nm for lithium like (Al XI) Al (Al^{10+}) ions, which belong to electric dipole transition radiation. The 989.01 nm spectral line for Ti XVIII (*i.e.* Ti^{17+}) de-excitation radiation belongs to magnetic dipole transition radiation. To our knowledge, these spectral lines are predicted by theoretical predictions from 1987 and 2013, and there have been no reports of experimental data so far.

The classical over-the-barrier model for the interaction between highly charged ions and metal solid targets in the Bohr velocity energy region has been validated. The trend of single particle fluorescence yield increasing with the potential energy of the incident ion is measured, which is roughly the same as the charge state trend of the incident ion rising with the potential energy (Fig. 3). The classical over-the-barrier model suggests that the charge state of the incident ion plays an important role in the ionization excitation of the target atom and the neutralization process of the target electron captured by the incident ion.

Conclusions   Highly charged ions are incident on a metal solid target surface and deposit the carried energy in the nano-space of the target surface within the femtosecond time scale, which ionizes and excites the target atoms and results in the emission of spectral lines. Some of the spectral lines are transitions between complex electronic configurations, leading to strong electric dipole forbidden transitions. There have been no experimental data reports on the 842.42 nm and 1525.03 nm spectral lines emitted by helium-like Al ions, as well as the 1251.08 nm spectral lines emitted by lithium-like Al ions, and the 989.01 nm spectral lines of Ti XVIII (*i.e.* Ti^{17+}) ion de-excitation radiation since the theoretical calculation results were published in 1987. The relative intensity of the spectral lines (single ion fluorescence production) we measure increases with the growing charge state of the incident ion, and the increasing trend is generally consistent with the potential energy trend of the incident ion increasing with the charge state. This indicates that the classical over-the-barrier model holds true in the energy region of the incident ion's kinetic energy near the Bohr velocity. The research methods for elastic and inelastic scattering caused by collisions between ions and gas target atoms are different. Due to many novel phenomena generated by highly charged ions incident on solid surfaces, such as the controversy over Auger and ICD processes, the energy shift caused by multiple ionization of target atoms, and the dissipation channels of total energy and gain energy of incident ions, a large quantity of work should be done. Meanwhile, we sincerely hope that our study can provide basic data and support for related research, and propose new methods for spectral measurement.